

# Revision 1

## Formation of hydrous stishovite from coesite in high pressure hydrothermal environments

Kristina Spektor<sup>1,\*\*</sup>, Johanna Nylén<sup>1</sup>, Renny Mathew<sup>1</sup>, Mattias Edén<sup>1</sup>, Emil Stoyanov<sup>2</sup>,  
Alexandra Navrotsky<sup>2</sup>, Kurt Leinenweber<sup>3</sup> and Ulrich Häussermann<sup>1,\*</sup>

<sup>1</sup>*Department of Materials and Environmental Chemistry, Stockholm University, SE-10691  
Stockholm, Sweden*

<sup>2</sup>*NEAT ORU, One Shields Avenue, University of California at Davis, Davis, CA 95616*

<sup>3</sup>*Department of Chemistry and Biochemistry, Arizona State University, Tempe, AZ 85287-1604*

<sup>\*\*</sup>*Present: ESRF, The European Synchrotron Radiation Facility, 38000 Grenoble, France*

Keywords: coesite-stishovite transition, hydrous minerals, octahedral defects, high-pressure hydrothermal environments

\*Email: [Ulrich.Haussermann@mmk.su.se](mailto:Ulrich.Haussermann@mmk.su.se)

28

## Abstract

29 In low temperature, high pressure hydrothermal environments coesite transforms into  
30 hydrous forms of stishovite. We studied hydrous stishovite produced from hydrothermal  
31 treatment of silica glass as initial SiO<sub>2</sub> source at temperatures of 350–550 °C and pressures  
32 around 10 GPa. The *p,T* quenched samples were analyzed by powder X-ray diffraction (PXRD),  
33 scanning electron microscopy (SEM), thermal analysis, IR and NMR spectroscopy. The presence  
34 of significant amounts of H<sub>2</sub>O (ranging from 0.5 to 3 wt%) is shown from thermogravimetric  
35 measurements. PXRD reveals that at temperatures below 400 °C hydrous stishovite is obtained  
36 as two distinct phases which may relate to the solid ice-VII environment present at prevailing *p,T*  
37 conditions. Initially formed hydrous stishovite is metastable and dehydrates over time in the low  
38 temperature, high pressure hydrothermal environment. The primary mechanism of H  
39 incorporation in stishovite is a direct substitution of 4H<sup>+</sup> for Si<sup>4+</sup> yielding unique octahedral  
40 hydrogarnet defects. In IR spectra this defect manifests itself by two broad but distinct bands at  
41 2650 and 2900 cm<sup>-1</sup>, indicating strong hydrogen bonding. These bands are shifted in the  
42 deuteride to 2029 and 2163 cm<sup>-1</sup>, respectively. Protons of the octahedral hydrogarnet defect  
43 produce <sup>1</sup>H MAS NMR signals in the 9–12 ppm region. The presence of multiple resonances  
44 suggests that the octahedral defect is associated with a variety of proton arrangements. At  
45 elevated temperatures NMR signals narrow considerably because of proton dynamics.

46

47

## 48 INTRODUCTION

49

50 Stishovite is an abundant mineral in the silica-rich sedimentary and basaltic parts of  
51 subducted oceanic slabs and crustal fragments at a wide range of depths in the Earth, spanning  
52 from the bottom of the upper mantle throughout the transition zone into the lower mantle (Ono et  
53 al. 2001; Hirose et al. 2005). At prevailing  $p, T$  conditions stishovite may contain up to 5%  $\text{Al}_2\text{O}_3$   
54 (Pawley et al. 1993; Smyth et al. 1995; Litasov et al. 2007). The substitution of  $\text{Al}^{3+}$  for  $\text{Si}^{4+}$  is  
55 partially charge balanced by protons, which creates OH groups, or structural water, in crystalline  
56 stishovite (Smyth et al. 1995; Gibbs et al. 2004; Bromiley et al. 2006). Al-bearing stishovite is  
57 considered an important carrier of water into the deep mantle (Litasov et al. 2007). Litasov et al.  
58 (2007) provided a detailed study of  $\text{Al}_2\text{O}_3$  solubility and the associated incorporation of protons  
59 in stishovite. Although there is a clear correlation between water and Al content in stishovite, it  
60 was found that  $\text{H}^+$  (OH groups) can only compensate for up to 40% of introduced  $\text{Al}^{3+}$ ; the  
61 majority of the  $\text{Al}^{3+}$  for  $\text{Si}^{4+}$  substitution is charge balanced by the formation of O vacancies. The  
62 maximum water content of Al-bearing stishovite is 3010 wt. ppm (0.3 wt%) (Litasov et al.  
63 2007).

64 In the absence of a trivalent cation, stishovite accepts only up to 50 wt.ppm of  $\text{H}_2\text{O}$ , and is  
65 classified as a nominally anhydrous mineral (NAM) (Pawley et al. 1993, Litasov et al. 2007). It  
66 has been speculated that  $\text{H}_2\text{O}$  incorporation in nominally Al-free stishovite is associated with a  
67 very low concentration of  $\text{Si}^{4+}$  vacancies (Bromiley et al. 2006). However, it is not clear whether  
68 nominally Al-free stishovite actually contains minor amounts of trivalent cations (Al, Fe) which  
69 are charge balanced by H. It came then as a surprise when low temperature, high pressure  
70 hydrothermal environments afforded hydrous stishovite with water contents exceeding 1 wt%,

71 that is three orders of magnitude higher than known previously for unsubstituted stishovite and  
72 one order of magnitude higher than for the Al-substituted variant (Spektor et al. 2011). Without  
73 the presence of other metals substituting for Si, the mechanism of hydrogen incorporation in  
74 hydrous stishovite is the hydrogarnet-like substitution  $4 \text{H}^+ \leftrightarrow \text{Si}^{4+}$ . And the presence of  
75 previously unknown octahedral hydrogarnet defects in large concentrations has been  
76 conclusively proven by NMR spectroscopy (Spektor et al. 2011).

77 It is uncertain whether octahedral hydrogarnet defects have wider implications as water  
78 storage mechanism in NAMs for Earth and planetary interiors. In any case, hydrous stishovite  
79 represents an interesting material with a rather unique bonding situation where 4  $\text{H}^+$  distribute  
80 over 6 O atoms, in contrast with conventional tetrahedral hydrogarnet defects as in grossular  
81 garnets where the four O atoms around a silicon vacancy are terminated as hydroxyl (Lager et al.  
82 1987; Rossman and Aines 1991; Kolesov and Geiger 2005). It also shows the potential of  
83 extreme hydrothermal environments for creating new materials. In this particular case, water acts  
84 as a catalyst (in the coesite – stishovite transition) and reactant (by being incorporated in  
85 stishovite) at the same time. In this work we follow up the initial discovery of hydrous stishovite  
86 (Spektor et al. 2011) and present a systematic description of the formation and characterization  
87 of samples obtained at 350–550 °C.

88

89

90

## 91 **EXPERIMENTAL METHODS**

92

### 93 **Synthesis**

94

95 55–65 mg of silica source and 20–35 mg Milli-Q purity water were loaded into cylindrical  
96 noble metal capsules (Au:Pd (80:20) and Ag:Pd (70:30) alloys, 6.2 mm length, 5 mm outer  
97 diameter). Capsules were sealed using a LaserStar 1900 laser welding station. The quality of  
98 seals was tested by heating capsules in an oven at 100 °C overnight and subsequent weighing.  
99 High pressure experiments were conducted in a 6-8 multi anvil device using an 18/12 assembly  
100 developed by Stoyanov et al. (2009). Capsules were inserted into a boron nitride sleeve and the  
101 BN sleeve was subsequently positioned in a graphite furnace. Samples were pressurized to 10  
102 GPa (800 metric tonnes of force) at 40 tonnes per hour and afterwards heated to a target  
103 temperature (between 350–550 °C) at a rate of about 20 °C/min and dwelled for typically 8 h.  
104 The temperature was measured close to the sample using a type C thermocouple (W5%Re –  
105 W26%Re wire) in an Al<sub>2</sub>O<sub>3</sub> sleeve. The temperature gradient was estimated to be about 20 °C  
106 along and 10 °C across the sample. After dwelling, samples were quenched by turning off the  
107 power to the furnace (~50 °C/sec), and the pressure was released at a rate of approx. 0.5 GPa/h.  
108 Recovered capsules were pinched open, verified to still contain free H<sub>2</sub>O, and the water then  
109 removed by evaporation at ~70 °C. The weight of the capsules was taken before and after the  
110 evaporation of the H<sub>2</sub>O. Occasional water loss (possibly due to microcracks) varied between 3  
111 and 10 mg (up to 10% of total sample mass).

112 Amorphous silica glass (SPEX, 99.999%) with a rather broad particle size distribution (2–  
113 200 µm) was used as the primary silica source. Additionally, single (cylindrical) pieces of silica

114 glass, silica glass with a narrow particle size distribution (around 1  $\mu\text{m}$ ), and coesite (prepared  
115 from silica glass at 5 GPa and 1000  $^{\circ}\text{C}$ ) were employed in control experiments. Table 1 lists the  
116 performed experiments most relevant to this work. Three experiments deviated from the general  
117 pattern: one run at 450  $^{\circ}\text{C}$  was terminated already after 15 min, one run at 450  $^{\circ}\text{C}$  employed  
118 heavy water ( $\text{D}_2\text{O}$ ) to investigate the possibility of synthesizing the deuterized form of hydrous  
119 stishovite, and lastly in one experiment a  $\text{SiO}_2$  glass/ $\text{H}_2\text{O}$  mixture was heated to 1000  $^{\circ}\text{C}$  during  
120 an hour, slowly cooled to 500  $^{\circ}\text{C}$  (1  $^{\circ}\text{C}/\text{min}$ ), and subsequently quenched to room temperature.  
121 Products were obtained as fine white powders which were used for further examination by  
122 powder X-ray diffraction, optical and NMR spectroscopy, and scanning electron microscopy.

123

#### 124 **Powder X-ray diffraction (PXRD) analysis**

125

126 For powder X-ray analysis of stishovite samples a Bruker D8 Advance and a Stoe Stadi P  
127 diffractometer were employed. Both instruments were equipped with a Ge-111 monochromator  
128 and operated in Debye-Scherrer geometry using  $\text{CuK}\alpha_1$  radiation. Stishovite samples were  
129 packed into 0.3 mm glass capillaries and measured during 9–12 hours at room temperature.  
130 These measurements covered a  $2\theta$  range 10–110 degrees with step sizes of either 0.008 or 0.015.  
131 Rietveld analysis (Rietveld 1969) of PXRD patterns was mainly performed with the Fullprof  
132 Suite (Rodriguez-Carvajal 1990). Patterns of the samples 350 and 450-15min were analyzed with  
133 the Topas software (AXS Bruker 2008). Structural data for the stishovite samples were obtained  
134 within the space group  $P4_2/mnm$ . The following parameters were refined: scale factor,  
135 background, unit cell dimensions, sample displacement, peak profile, atomic coordinates of  
136 oxygen atoms, isotropic atomic displacement parameters ( $B_{\text{iso}}$ ), absorption correction (in Topas

137 according to Sabine et al. (1998); in Fullprof  $\mu R$  was fixed to 1 for every pattern), anisotropic  
138 peak broadening using spherical harmonics (Järvinen 1993) and peak asymmetry. For the  
139 Rietveld analysis using Fullprof, starting values for  $B_{iso}$  were taken from the paper by Endo et al.  
140 (1986) and kept fixed during the refinement, being only released by the end of it. Pseudo-Voight  
141 or Thompson-Cox-Hastings Pseudo-Voight functions were used for the peak shape refinement.

142

### 143 **Scanning electron microscopy (SEM) investigations**

144

145 SEM studies were performed using an JEOL JSM 7000F instrument equipped with a  
146 Schottky-type field emission gun. Stishovite samples were mounted to an aluminum stub using  
147 carbon tape and partially coated with a gold layer of 10–15 nm thickness to improve the  
148 conductivity. Uncoated sample areas were preserved to ensure that no visible surface  
149 peculiarities arise from the presence of gold nanoparticles. For imaging typically an accelerating  
150 voltage of 3 kV, a probe current  $<10$  pA and an 8 mm working distance was used.

151

### 152 **Vibrational Spectroscopy**

153

154 Raman spectra were acquired at room temperature using the excitation line of 532 nm from a  
155 Compass 315-M laser (Coherent, Inc.). The scattered light was collected in backscattering  
156 configuration into an Acton SpectraPro 300i spectrometer (Princeton Instruments) after  
157 removing the laser light by using a laser bandpass filter followed by an edge filter. The signal  
158 was then diffracted off a 1200 grooves  $\text{mm}^{-1}$  grating and collected into a back-thinned, liquid

159 nitrogen cooled Princeton Instruments detector. The system has a spectral resolution of about 2  
160  $\text{cm}^{-1}$ . A laser power of 70 mW was used and the accumulated collection time was 60 seconds.

161 Fourier-transform infrared spectra (FTIR) were acquired on Bruker IFS 66v/s and Varian  
162 610-IR FT-IR spectrometers in the 400–4000  $\text{cm}^{-1}$  wavenumber range (128 scans, resolution 4  
163  $\text{cm}^{-1}$ ). The former instrument was employed for transmission measurements using KBr pellets  
164 with an approximate ratio of stishovite and KBr 1:100. Attenuation total reflection (ATR) spectra  
165 were recorded with the latter instrument using a Specac Goldengate micro-ATR accessory  
166 equipped with KRS-5 lenses and a diamond ATR element. Spectra were baseline-corrected and  
167 normalized in a range from 0 to 1. FTIR spectra at elevated temperatures were collected using a  
168 Varian 610-IR microscope in reflection mode connected to a Varian 670-IR spectrometer. The  
169 stishovite sample was placed on an Al foil in order to ensure accurate temperature control, and  
170 the latter was loaded onto a Linkam THMS600 heating stage equipped with a water cooling  
171 system and a temperature controller connected to a computer. Temperature was varied from 25  
172 to 300 °C with a heating rate of 25 °C/min.

173

#### 174 **Thermal analysis**

175

176 Thermogravimetric analysis and differential scanning calorimetry (TGA/DSC) were carried  
177 out using a Netzsch STA 449 system. The samples (5–8 mg powders) were heated in a platinum  
178 crucible from room temperature to 1000 °C in argon with a heating rate of 10 °C/min. A  
179 buoyancy correction was made by subtracting the baseline collected by running a blank  
180 TGA/DSC with an empty platinum crucible. The water content was determined by the TGA  
181 weight loss curves and by weighing the samples on a microbalance before and after the  
182 experiment.

## 183 **Solid-State Nuclear Magnetic Resonance (NMR) Spectroscopy**

184

185 Magic-angle spinning (MAS)  $^1\text{H}$  NMR experiments were performed at an external magnetic  
186 field of 14.1 T, by using a Bruker Avance-III spectrometer operating at a  $^1\text{H}$  Larmor frequency  
187 of  $-600.1$  MHz. A powder of the 450-C hydrous stishovite specimen was packed in a 3.2 mm  
188 zirconia rotor and spun at 24.00 kHz. The  $^1\text{H}$  NMR acquisitions utilized excitation by  $90^\circ$  pulses  
189 that operated at 90 kHz nutation frequency. The background suppression method introduced by  
190 Jaeger and Hemmann (2014) was employed for removing the  $^1\text{H}$  background signals from the  
191 NMR probe head.  $^1\text{H}$  NMR spectra were acquired at  $30^\circ\text{C}$  and  $110^\circ\text{C}$ , with relaxation delay of  
192 60 s and 128 accumulated signal transients at each temperature. Signal apodization equivalent to  
193 a 100 Hz of Lorentzian broadening was applied before Fourier transformation.  $^1\text{H}$  chemical shifts  
194 are quoted relative to neat tetramethylsilane. Essentially identical NMR spectra at  $30^\circ\text{C}$  were  
195 obtained before and after heating, evidencing the absence of any irreversible chemical/physical  
196 transformation of the sample during the heating cycle. The Boltzmann-dictated temperature  
197 dependence leads to slightly different total integrated NMR intensities at  $30^\circ\text{C}$  and  $110^\circ\text{C}$ .

198

199

## 200 **RESULTS AND DISCUSSIONS**

201

### 202 **Formation of hydrous stishovite**

203

204 Mixtures of silica glass and water with an approximate molar ratio of 1:1 were compressed to  
205 10 GPa and subsequently heated to a temperature between  $350$  and  $550^\circ\text{C}$  at a rate of  $20^\circ\text{C}/\text{min}$ .

206 In a typical experiment the silica-water mixture was equilibrated for 8 hours prior to  $p,T$   
207 quenching (cf. Table 1). Because the melting point of ice-VII at 10 GPa is near 425 °C (700 K)  
208 (Datchi et al. 2000; Dubrovinskaia 2003; Lin et al. 2004), the water environment was expected to  
209 be solid for experiments at 350 °C and 400 °C. It is well established that water catalyzes the  
210 transformation of amorphous silica to coesite, which proceeds via the intermediate phase of  
211 quartz (Kameyama et al. 1974; Naka et al. 1974a, 1974b; Zhang et al. 2008; Arasuna et al.  
212 2013). Studies at 3 GPa by Naga et al. (1974a, 1974b) showed that in the presence of free, liquid,  
213 water, the transformation can be accelerated by several orders of magnitude. Additionally, free  
214 water will act as a mineralizer, promoting the growth of euhedral crystals with well-developed  
215 faces. The catalytic effect of water is also demonstrated in the synthesis of coesite from hydrous  
216 forms of amorphous silica, such as silica gel and hydrous silica glass, which can be achieved at  
217 temperatures as low as 100 °C (Zhang et al. 2008; Arasuna et al. 2013). Thus, in our experiments  
218 we expect that when heating the silica–water mixture at 10 GPa, an initial conversion to coesite  
219 takes place.

220 Figure 1 shows the evolution of products for the temperature interval 350–550 °C during 8  
221 hour experiments. At 350 °C the sample corresponded to a mixture of stishovite with a small  
222 fraction of coesite (about 15%). Products obtained at 400–550 °C were coesite-free stishovite.  
223 The Bragg positions of reflections from hydrothermally produced stishovite deviate significantly  
224 from those of regular stishovite, particularly in the  $hk0$  set. Obviously, water incorporation leads  
225 to an increased  $a$  lattice parameter of the tetragonal unit cell. It is also noticeable that compared  
226 to anhydrous stishovite reflections are considerably broadened and that the broadening seems to  
227 increase when applying lower dwelling temperatures. A closer inspection of the PXRD patterns  
228 from the 350 and 400 samples revealed that they are actually composed of two distinct phases of

229 hydrous stishovite. The slow cooling experiment from 1000 °C resulted in regular, anhydrous  
230 stishovite. The PXRD pattern from this sample is contained in Figure 1.

231 The trend in the PXRD patterns is best detailed in the variation of the 220 reflection, which is  
232 shown in Figure 1b. This reflection is split in the two-phase patterns of the 350 and 400 samples,  
233 and corresponds to a single, but broad, peak in the pattern of the 450 °C product. The peak width  
234 of the 220 reflection is then significantly reduced in the patterns of the 500 and 550 samples. The  
235 shoulder at lower angles in the 500 pattern indicates phase heterogeneity. The peak position in  
236 both patterns is very similar and, compared to the 450 pattern, considerably shifted toward  
237 anhydrous stishovite. That is, with increasing dwelling temperature, the *a* lattice parameter of  
238 anhydrous stishovite is approached.

239 It is important to point out that (i) the formation of hydrous stishovite and (ii) its occurrence  
240 as two distinct phases at lower temperatures is independent of the initial silica source employed  
241 in the hydrothermal high pressure treatment. The silica glass applied for most reactions displayed  
242 a rather broad distribution of particle sizes (2–200 μm). Control experiments using silica glass  
243 with a very narrow particle size distribution around 1 μm and as rod-shaped single pieces did not  
244 show noticeable differences in the stishovite products, according to PXRD and SEM analysis.  
245 Hydrous stishovite can also be obtained when using coesite as silica source. This has been shown  
246 earlier for dwelling experiments at 450 °C which yielded single phase products (Spektor et al.  
247 2011). Here we show that – as for silica glass – dwelling experiments at 400 °C afford two  
248 phases of hydrous stishovite (Figure 2a). Deuterized hydrous stishovite can be produced when  
249 using a high pressure D<sub>2</sub>O environment. Dwelling at 450 °C resulted in a pronounced two phase  
250 product (Figure 2a). It is not clear whether this is due to D<sub>2</sub>O or an inaccurate temperature  
251 measurement in this run.

252 The formation of hydrous stishovite follows from the coesite – stishovite transition in the  
253 presence of a (large) excess of free water. As for the amorphous silica – coesite transformation  
254 water also catalyzes the coesite – stishovite transition. The critical temperature for determining  
255 the coesite-stishovite equilibrium phase boundary is about 1000 °C (Zhang et al. 1996). The  
256 presence of free water lowers the kinetic barrier decisively and stishovite was obtained at  
257 unprecedented low temperatures. Note, that control experiments using silica glass in a dry  
258 environment at 10 GPa and 8 h dwelling time did not indicate any transformation up to 550 °C.  
259 The formation of hydrous stishovite implies that water acts as catalyst and reactant at the same  
260 time. This is different to the hydrothermally assisted amorphous silica – coesite transformation,  
261 which does not lead to structural water incorporation. To obtain some information about the  
262 reaction rate for the coesite – hydrous stishovite transition we performed an experiment at 450  
263 °C that was quenched after only 15 min (run 450-15min). The total heating time corresponded to  
264 about 35 min. The PXRD pattern of the product is included in Figure 2a, showing an almost  
265 completed transformation to a single phase hydrous stishovite. The phase fractions determined  
266 from Rietveld analysis are 88% hydrous stishovite and 12% coesite.

267 Runs at 450 °C appear special. In contrast with dwelling at 400 °C they seemed to afford  
268 (with the exception of the 450-D2O experiment) single phase stishovite products, and compared  
269 to runs at 500 and 550 °C Bragg positions are at distinctly lower  $2\theta$  values. Figure 2b shows the  
270 variation of the 220 reflection for products obtained at 450 °C, in comparison with the 400 and  
271 500 samples. Interestingly, sample 450-10h turned out to be heterogeneous, in a similar way as  
272 sample 500. We further note that the 220 reflection of sample 450-15min is shifted significantly  
273 to lower angles compared to 450-8h. This strongly indicates that initially formed hydrous  
274 stishovite dehydrates over time. The end point of this progression (>10 hours) may be anhydrous

275 stishovite, but this is presently unknown. In this respect, prolonged dwelling and increased  
276 temperature seem to act in the same direction. Phase heterogeneity of the samples 450-10h and  
277 500 may indicate that during dehydration a phase segregation, into a more and less hydrous form  
278 (termed “h+” and “h-“, respectively (cf. Tables 1 and 2)) takes place and less stable h+ dissolves  
279 during ripening and further dehydration of h-. This however is speculative. Also, at this point, we  
280 are not able to explain the two-phase phenomenon at lower temperatures. However, we make the  
281 conjecture that it relates to a solid water environment present at prevailing  $p,T$  conditions. It is  
282 clear that processes at 350 and 400 °C will differ from those at higher temperatures because  
283 dissolution and mass transport of SiO<sub>2</sub> is prohibited.

284 Figure 3 depicts SEM images for the samples 350–550, showing the effect of increasing  
285 dwelling temperature. In the 350 °C product stishovite is obtained as fine, dendritic, 0.2–0.5  
286 micrometer sized crystals, held together in large agglomerates which resemble the glass pieces in  
287 the starting material. The crystals are peculiarly intergrown with apparently two primary  
288 orientations. The overall texture is most likely a result of the microstructure of coesite domains  
289 obtained from the initial hydrothermal transformation of the glass. In the 400 °C product  
290 agglomerates of stishovite crystals are smaller and the regularly interwoven pattern seen in  
291 sample 350 is absent. Also, the size of crystals is larger than in sample 350 and dimensions reach  
292 1 micrometer. The larger crystal dimensions must be attributed to initially larger coesite  
293 crystals/domains. Hydrous stishovite crystals are platelet-shaped with thin round edges and  
294 thicknesses far below 0.1 micrometer. The presence of two distinct stishovite phases in the  
295 samples 350 and 400, as clearly evidenced from PXRD, cannot be reconciled in the SEM  
296 images.

297 In the sample 450 previously intergrown crystals are largely separated with the former  
298 intergrowth contacts clearly noticeable. The size and shape of stishovite crystals resemble those  
299 for sample 400, but a part of them have developed sharp corners and thicker edges. This  
300 indicates ripening due to enhanced mass transport in a liquid water environment. The solubility  
301 of silica at these conditions should correspond to that of metastable coesite (which is unknown,  
302 but has to be higher than that of stishovite which is very low ( $\ll 1$  wt%) (Shatskiy et al. 2010).  
303 Crystals obtained at higher temperatures (500 °C and 550 °C) are clearly thicker and more  
304 homogenous in size and shape. Additionally, crystal surfaces started developing into distinct  
305 faces. The crystals of sample 550 have a rather uniform size and morphology. Anhydrous  
306 crystals obtained from the slow cooling experiment display well defined faces and sharp edges.  
307 Their elongated prismatic shape is similar to anhydrous stishovite grown in high temperature  
308 hydrothermal environments by Lityagina et al. (2001) and Shatskiy et al. (2010).

309 Most instructive is the 450-15min experiment because it provides a snapshot of the early  
310 stage of stishovite formation. Although stishovite was obtained “single phase” according to  
311 PXRD (cf. Figure 2b), the sample appears heterogeneous in SEM (Figure 4). Parts of the sample  
312 resemble strongly crystals in the sample 400, suggesting the same transformation mechanism  
313 from initially intergrown coesite. It is also clearly seen that the liquid water environment  
314 promotes the growth of coesite crystals prior to transformation to hydrous stishovite. That is,  
315 coesite crystal ripening competes with transition into hydrous stishovite. Sample 450-15min  
316 contains well developed coesite crystals, 2–4  $\mu\text{m}$  in size, with small bulky rounded crystals  
317 attached to it, suggesting Ostwald ripening. From ripened coesite crystals, hydrous stishovite  
318 crystals of square tabular shape can be seen peeling off.

319 We conclude this section by summarizing our observations concerning the formation of  
320 hydrous stishovite near 10 GPa:

321 (i) Hydrous stishovite forms in hydrothermally assisted transitions of coesite to stishovite  
322 when employing excess water and low temperatures. Water acts as catalyst and reactant.  
323 Presumably, temperatures above 600 °C will produce anhydrous stishovite. Our slow cooling  
324 experiment from 1000 °C and previous high temperature experiments in an excess water  
325 environment (Lityagina et al. 2001; Shatsky et al. 2010) produced anhydrous stishovite. When  
326 exposing a sample of anhydrous stishovite to hydrothermal conditions at 10 GPa and 450 °C for  
327 8 hours, hydration was not observed.

328 (ii) Independent of the initial SiO<sub>2</sub> source, two phases of hydrous stishovite were obtained at  
329 350 and 400 °C, which is attributed to a solid water environment. It is not clear why this  
330 phenomenon occurs. It is also not clear why it has been observed with D<sub>2</sub>O at 450 °C. Phase  
331 heterogeneities were also observed in samples produced at liquid water temperatures.

332 (iii) Hydrous stishovite is metastable and dehydrates over time in a high pressure  
333 hydrothermal environment. It is not clear whether the end point corresponds to anhydrous  
334 stishovite.

335 To settle the many open questions concerning formation and metastable nature of hydrous  
336 stishovite will require investigations into the evolution of products with dwelling time at various  
337 temperatures and perhaps also pressures. With respect to formation, in-situ studies at synchrotron  
338 beamlines would be very valuable.

339

340 **Thermal behavior of hydrous stishovite**

341

342 The mechanism for water incorporation in hydrous stishovite is the hydrogarnet defect where  
343 a cluster of four OH<sup>-</sup> ([OH<sup>-</sup>]<sub>4</sub>) replaces an entity SiO<sub>4</sub><sup>4-</sup>, or alternatively four protons H<sup>+</sup> substitute  
344 one Si<sup>4+</sup>. Hydrogarnet defects are especially established for tetrahedrally coordinated Si in  
345 grossular garnets (Rossman and Aines 1991, Kolesov and Geiger 2005). They have been never  
346 reported for octahedrally coordinated Si. Octahedral defects as mechanism for H incorporation in  
347 hydrous stishovite has been firmly established from <sup>29</sup>Si and <sup>1</sup>H MAS NMR experiments in our  
348 previous work (Spektor et al. 2011).

349 To assess water contents, hydrous stishovite samples were subjected to thermogravimetric  
350 analysis (TGA). Previously it was shown for the sample 450 that the weight loss determined by  
351 TGA agrees within uncertainties with H analysis by secondary ion mass spectrometry (Spektor et  
352 al. 2011). Figure 5 compares differential scanning calorimetry (DSC) and TGA traces of  
353 anhydrous and various hydrous stishovite samples. Dry stishovite decomposes exothermically  
354 into a glass at around 550 °C. The small weight loss of 0.2% below 300 °C in all samples is  
355 attributed to surface water/hydroxyl. The shape of the DSC traces for samples 450, 500 and 550  
356 (the latter is not shown) is similar to that for anhydrous stishovite, with a sharp rise and a distinct  
357 maximum. The onset of decomposition, however, is shifted to lower temperatures. For the 450  
358 sample it is around 500 °C. The two-phase sample 400 is clearly different: its DSC signal  
359 extends over more than 200 °C and has a broad maximum. The onset temperature is below 400  
360 °C.

361 Coinciding with the decomposition onset seen in DSC, the TGA traces of hydrous samples  
362 show a sharp discontinuity which is associated with considerable weight-losses upon release of  
363 structurally bonded water. These weight-loss amounts to 0.65 and 0.7% for the 500 and 550  
364 samples, respectively, and to 1.4% for the 450 sample. For the two-phase 400 sample it is near 3

365 wt%. Even if TGA results are usually associated with larger uncertainties with respect to the  
366 precise content of structural water (Rossman 2006) – and for our particular samples we need also  
367 to consider contamination with an unknown (small) amount of silicic acid from dissolved silica  
368 in the water environment that precipitates upon evaporation – these investigations indicate that  
369 several wt% of water can be incorporated in stishovite. Metastable hydrous stishovite and its  
370 decomposition can be expressed with the formula  $\text{Si}_{1-x}\text{H}_{4x}\text{O}_2 = (1-x) \text{SiO}_2 + 2x \text{H}_2\text{O}$ . 3 wt% of  
371 water would correspond to a Si defect concentration of almost 5% ( $x = 0.05$ ).

372

### 373 **Structural variations of hydrous stishovite**

374

375 As shown in Figures 1 and 2, the PXRD patterns of hydrous stishovite show systematic  
376 deviations from anhydrous stishovite. Because of the increased  $a$  lattice parameter, reflections  
377 with higher  $h$  and  $k$  values are shifted pronouncedly to lower Bragg angles. For examining the  
378 structural changes in more detail, the PXRD patterns of hydrous stishovite samples were  
379 subjected to Rietveld analysis. Refinements were based on the conventional space group of  
380 stishovite ( $P4_2/mnm$ ). Symmetry lowering is not supported from our PXRD data. However,  
381 patterns of all the hydrous samples exhibit noticeable anisotropic line broadening, which seemed  
382 to get more severe for samples obtained at lower temperatures. In order to account for this issue,  
383 a spherical harmonics model was introduced (the order was kept as low as possible). The  
384 refinement results are compiled in Table 2 which also contains the structural parameters of  
385 anhydrous stishovite obtained from the slow cooling experiment (cf. Table 1). As mentioned  
386 earlier, a water content of 3 wt% would translate to a Si defect concentration of about 5%, which  
387 suggests occupational deficiency of the Si atom site. However, because of the significant

388 anisotropic peak broadening as well as uncertainties in mass absorption coefficients affecting the  
389 thermal parameters, it was not possible to reliably refine the site occupancy of Si and O atoms.  
390 Instead they were constrained to 1.

391 Generally, refinements yielded satisfactory reliability factors. This included the two-phase  
392 samples (where atomic displacement parameters of silicon and oxygen atoms were constrained).  
393 Figure 6a shows the Rietveld plot of the pattern for the sample 400. Also patterns of samples  
394 with phase heterogeneity (samples 450-10h and 500) were treated favorably as two phase  
395 models. This is shown for the 500 sample. The pronounced hkl-dependent peak asymmetry of  
396 the PXRD pattern can not be resolved within a single phase refinement (Figure 6b). Including a  
397 second phase with a larger unit cell accounts for the asymmetry and improved the Rietveld fit  
398 (Figure 6c, Table 2).

399 The rutile-type stishovite structure (shown in Figure 7a) has three structural parameters, the  
400 tetragonal unit cell parameters  $a$  and  $c$ , and the position parameter of the O atom located on  
401 Wyckoff position 4f ( $x,x,0$ ). Whereas the  $c$  lattice parameter remains largely unaffected the  $a$   
402 parameter may increase by almost 1% in the hydrous forms. This amounts to a volume increase  
403 exceeding 2%. The largest  $a$  parameters are observed for the more hydrous phase (termed “h+”  
404 in the two phase samples obtained at 400 and 350 °C. The O atom position parameter appears to  
405 have a tendency to increase with increasing  $a$  lattice parameter. In the stishovite structure there  
406 are three different nearest neighbor O–O distances (corresponding to the edges of  $\text{SiO}_6$   
407 octahedra) and two Si–O distances (Figure 7b). In hydrous stishovite two of these distances ((O–  
408 O)<sub>2</sub> and (Si–O)<sub>2</sub>, cf. Figure 7b) increase noticeably, accounting for a slight elongation of  $\text{SiO}_6$   
409 octahedra along the (pseudo) fourfold axis parallel the  $ab$  plane.

410 Obviously, conventional Rietveld refinement of PXRD data will just deliver average  
411 structures with respect to Si and O atoms. No information is obtained about the arrangement of  
412 protons within the octahedral hydrogarnet defect, which represents an interesting bonding  
413 situation where 4 protons distribute over 6 O atoms. True insight into the distribution of protons  
414 within defects could be gained from the analysis of pair distribution functions extracted from  
415 neutron total scattering measurements of deuterized samples. A problem for neutron scattering  
416 investigations is the rather small amount of sample obtained from multi-anvil synthesis and the  
417 comparatively low concentration of hydrogen. However, the intense neutron beams at the  
418 spallation source SNS at ORNL may enable structure elucidation of the octahedral hydrogarnet  
419 defect in future neutron scattering studies. In the following we focus on the vibrational  
420 spectroscopy characterization of this defect.

421

#### 422 **Spectroscopic characterization of the octahedral hydrogarnet defect**

423

424 For rutile-type stishovite Raman and IR spectra are truly complementary (Hemley et al.  
425 1986). Raman spectroscopy exclusively probes Si atom displacements whereas IR active modes  
426 involve Si–O vibrations. The location of the bands for the four fundamental Raman active modes  
427  $B_{1g}$ ,  $E_g$ ,  $A_{1g}$ , and  $B_{2g}$  is virtually identical for anhydrous and hydrous stishovite (Figure 8a).  
428 Those bands are however considerably broadened in the spectrum of the latter. Likewise there  
429 are 4 IR active modes,  $E_u(1)$ ,  $E_u(2)$  and  $E_u(3)$ , and  $A_{2u}$ , which have an LO and TO component  
430 each (Hofmeister et al. 1990; Lee and Gonze 1994). In our IR spectra only the  $E_u$  bands are  
431 clearly detected (Figure 8b). In the hydrous materials, bands corresponding to Si-O vibrations are  
432 slightly red shifted, by 5 to 10  $\text{cm}^{-1}$  for the 550 and 500 samples, by about 20  $\text{cm}^{-1}$  for the 450

433 samples, and up to  $30 \text{ cm}^{-1}$  for the two-phase samples 400 and 350. At the same time the  
434 intensity of the  $E_u(2)$  band at around  $600 \text{ cm}^{-1}$  diminishes. The red shift can be attributed to the  
435 slightly increased Si-O distances in hydrous stishovite (cf. Figure 7b).

436 O-H vibrations could not be observed in Raman, but they are clearly visible in the region  
437  $2400\text{--}3500 \text{ cm}^{-1}$  of the IR spectrum which is dominated by two broad bands at 2650 and 2900  
438  $\text{cm}^{-1}$  (Figure 9a). We assign these bands to the octahedral hydrogarnet defect. It is not clear if the  
439 two bands originate from independent or coupled OH vibrations. (Note that the tetrahedral  
440 hydrogarnet defect manifests itself with a single OH stretching band (Rossman and Aines 1991)).  
441 When assuming independent oscillators and correlating the wavenumbers 2650 and  $2900 \text{ cm}^{-1}$   
442 with [O-H $\cdots$ O] distances according to Libowitzky (1999) one obtains  $d_{\text{O}\cdots\text{O}} = 2.59$  and  $2.63 \text{ \AA}$ .  
443 These values reflect the two longer O–O distances in the stishovite crystal structure (i.e. 2.52,  
444  $2.65 \text{ \AA}$ , cf. Figure 6b). Likewise, the Libowitzky correlation suggests H $\cdots$ O distances  $d_{\text{H}\cdots\text{O}} = 1.6$   
445 and  $1.7 \text{ \AA}$ . The so extracted bond lengths for O $\cdots$ O and H $\cdots$ O are both associated with strong  
446 hydrogen bonding.

447 The assignment of bands at 2650 and  $2900 \text{ cm}^{-1}$  to the octahedral defect is corroborated by the  
448 spectrum of the deuterized sample (Figure 9b). The double peak is shifted to 2029 and  $2163 \text{ cm}^{-1}$ ,  
449 corresponding to the isotope shifts 1.31 and 1.34 which indicates significant anharmonicity, as  
450 expected for strong H bonded systems (Wöhlecke and Kovacs 2001). Bands are sharper in the  
451 450-D<sub>2</sub>O spectrum which is typical because of the reduced anharmonicity of O–D stretching  
452 vibrations in comparison to O–H modes. In addition to the pronounced double peak there is a  
453 weak band at  $3390 \text{ cm}^{-1}$  in the spectra of samples obtained at temperature  $450 \text{ }^\circ\text{C}$  and above (i.e.  
454 in a liquid water environment). The nature of this band was not clear in our previous work  
455 (Spektor 2011), here we attribute it to OH from small amounts of water inclusions in grain

456 boundaries (intergranular water). Finally, there is an intense and sharp band near  $1420\text{ cm}^{-1}$   
457 (outside the wavenumber region of OH stretching) whose origin is unknown. It may relate to OH  
458 bending associated with the octahedral defect. This band may be also present in the spectrum of  
459 the 450-D2O sample as a shoulder near  $1079\text{ cm}^{-1}$ . Note, that the spectrum of 450-D2O contains  
460 as well weak O–H bands, and the band at  $1383\text{ cm}^{-1}$  may relate to the presence of H.

461 Figure 10 compiles temperature dependent IR spectra of sample 450 which were collected up  
462 to  $300\text{ }^{\circ}\text{C}$ . As expected from the TGA investigation, the sample stayed intact and also no  
463 structural transformation is apparent. With temperature the double peak of the octahedral defect  
464 is slightly red shifted (and so is the ominous peak near  $1420\text{ cm}^{-1}$ ). The band near  $3390\text{ cm}^{-1}$  is  
465 lost at  $150\text{ }^{\circ}\text{C}$  which supports its assignment as OH from water inclusions.

466 We point out that the O-H wavenumber region of the IR spectrum of hydrous stishovite  
467 appears very different compared to nominally anhydrous stishovite with up 50 wt.ppm water and  
468 Al-bearing stishovite with up to 3000 wt.ppm (0.3 wt%) water. Their IR spectra are similar and  
469 characterized by an intense, broad and anisotropic band in the region  $3111 - 3134\text{ cm}^{-1}$  and  
470 various weak features at around  $3240$  and  $3312\text{ cm}^{-1}$  (Bromiley et al. 2006, Litasov et al. 2007,  
471 Thomas et al. 2009). However, Litasov et al. (2007) reported on a seemingly previously  
472 undetected band at  $2667\text{ cm}^{-1}$ , which may relate to octahedral defects. Furthermore, there is also  
473 no similarity with the IR spectrum of hydrogrossular where tetrahedral hydrogarnet defects give  
474 rise to a single OH absorption at around  $3662\text{ cm}^{-1}$ , indicating very weak hydrogen bonding  
475 (Libowitzky and Beran 2006). This underlines the drastically different bonding situation between  
476 octahedral and tetrahedral defects. In the former four protons coordinate 6 O atoms, which leads  
477 to weakened primary O-H bonds and strong hydrogen bonding [O-H $\cdots$ O], whereas in the latter  
478 the four O atoms are terminated regularly as hydroxyl and, thus, hydrogen bonding is weak.

479

480 Figure 11 displays  $^1\text{H}$  MAS NMR spectra collected from hydrous stishovite at two different  
481 temperatures, 30 °C (red trace) and 110 °C (black trace). The spectrum recorded at 30 °C is  
482 similar to that previously presented by Spektor et al. (2011) from a sample derived from  
483 amorphous silica, and referred to as “450-G”. NMR signals around 1-2 ppm and 5 ppm are  
484 attributed to surface hydroxyl species and intergranular water inclusions, respectively.  
485 Noteworthy, intergranular water inclusions are especially pronounced when sintered coesite is  
486 applied as starting material in the synthesis of hydrous stishovite; this accounts for the stronger  
487  $^1\text{H}$  NMR intensity  $\sim 5$  ppm from the sample “450-Co” used in Spektor (2011) relative to the  
488 present hydrous stishovite specimen that only reveals a weak resonance  $\sim 5$  ppm. As none of the  
489 NMR signals in the 0–5 ppm region (Figure 11) involve sites of the stishovite structure, they are  
490 henceforth ignored.

491 The  $^1\text{H}$  resonances of the octahedral defect appear in the 9–12 ppm spectral region and  
492 comprises (at least) three main, but heavily overlapping, peak components; see Figure 11. This  
493 suggests that the octahedral hydrogarnet defect does not involve one unique proton site (and  
494 thereby a single resonance), but rather represents energetically similar proton configurations  
495 associated with several distinct chemical shifts. The strikingly different NMR spectra at the two  
496 temperatures—with a clear signal-narrowing observed when the temperature was increased—  
497 unambiguously reveals the presence of proton dynamics. The resonance-narrowing appears to  
498 stem primarily from redistributions of the various proton populations in the structure, as reflected  
499 in altered intensities among the associated NMR peak components (and possibly also their  
500 widths). For instance, the two resonances at  $\sim 9.4$  ppm and  $\sim 10.8$  ppm appear in both spectra.  
501 However, the (broad) signal  $\sim 9.4$  ppm is relatively intense in the NMR spectrum obtained at 30

502 °C, whereas at 110 °C, this signal is weak and merely occurs around the base of the main  
503 resonance at 11.1 ppm. Similarly, while the peak ~10.8 ppm is clearly visible at 30 °C, at 110 °C  
504 it is only discernible as a shoulder of the main resonance (cf. Figure 11b). Besides the markedly  
505 different relative peak intensities, the main distinction between the two NMR data sets appears to  
506 be an overall shift in the *position* of the resonance from 11.4 ppm (at 30 °C) to 11.1 ppm at 110  
507 °C. We emphasize that whereas the NMR results unambiguously prove the presence of proton  
508 dynamics, which involves changes in the populations of the various proton configurations when  
509 the temperature is altered, no further information about the type of proton mobility is revealed.  
510 Note, that the strong hydrogen bonding (weakened primary O-H bonds) within an octahedral  
511 defect should facilitate proton dynamics. Deeper insight has to come from <sup>1</sup>H NMR  
512 investigations covering a much wider temperature range and computational modeling.

513

514

## 515 **CONCLUSIONS**

516

517 The hydrothermal treatment of SiO<sub>2</sub> at high pressures catalyzes the coesite – stishovite  
518 transition and produces hydrous forms of stishovite. At pressures around 10 GPa the formation  
519 of stishovite is already observed at temperatures below 350 °C. However, to obtain significant  
520 rates temperatures above 400 °C are needed, which presumably coincides with the melting of ice  
521 VII. Also, at temperatures below 400 °C a two-phase mixture (h<sup>+</sup> and h<sup>-</sup>) is obtained. The  
522 mechanism behind the formation of hydrous stishovite is not clear, but it appears that water is  
523 incorporated at the same time coesite with tetrahedrally coordinated Si transforms to denser  
524 stishovite (“transformation-reaction”). Hydrous stishovite is metastable and dehydrates over time

525 at high pressure hydrothermal conditions. Unique with hydrous stishovite is the amount of water  
526 incorporated ( $> 1$  wt%) and the substitution mechanism via unprecedented octahedral  
527 hydrogarnet defects. The octahedral hydrogarnet defect manifests itself as double peak at 2650  
528 and  $2900\text{ cm}^{-1}$  in IR spectra and with resonances near 11 ppm in  $^1\text{H}$  MAS NMR spectra. Clearly,  
529 the octahedral defect represents a new and complex bonding situation. The elucidation of its  
530 structural properties and dynamic behavior will be challenging and has to involve neutron  
531 scattering techniques, in particular total diffraction for pair distribution analysis and inelastic  
532 neutron scattering for conclusive vibrational property characterization, multiple temperature  
533 NMR investigations as well as molecular dynamics computational modeling. Further, there  
534 needs to be additional studies into the conditions of formation and metastable nature of hydrous  
535 stishovite. This includes detailed characterization of the solubility of water in stishovite as a  
536 function of temperature, pressure, as well as dehydration kinetics.

537

538

## 539 **IMPLICATIONS**

540

541 The unexpected discovery of hydrous stishovite shows the potential of low temperature, high  
542 pressure hydrothermal environments for creating new materials. There have been very few  
543 reports on the application of such environments at pressures approaching 10 GPa, yet these  
544 conditions may be significant in Earth and planetary settings. For example, conditions of 450–  
545 550 °C and 9–10 GPa can occur during the subduction of old, cold oceanic crust (Hacker et al.  
546 2003), including in the eclogitic former oceanic crustal layer which contains free  $\text{SiO}_2$  at these  
547 pressures (Ricolleau et al. 2010). Under these cooler conditions, dehydration reactions such as

548 serpentine are still occurring (Hacker et al. 2003) which will provide H<sub>2</sub>O that could then react  
549 with coesite to initially form hydrous stishovite. Rocks exhumed by natural processes from these  
550 environments have been found to contain coesite, and some are suggested to contain relicts of  
551 stishovite (Liu et al. 2007). Furthermore, the rich variety of *p,T* environments inferred for the  
552 ever-growing number of discovered exoplanets may include rather cool high-pressure  
553 environments which, in the presence of water, may result in hydrothermal conditions similar to  
554 those studied here. Finally, the octahedral hydrogarnet defect should be explored as a general  
555 hydrogen storage mechanism in other nominally anhydrous silicates containing octahedral  
556 silicon in Earth and planetary interiors (e.g., silicate garnet, perovskite, postperovskite phases).

557

558

559 **Acknowledgements.** This work was supported by the Swedish Research Council (VR) and the  
560 US National Science Foundation (NSF) through Grants 2013-4690 and DMR-1007557,  
561 respectively.

562

563

564

565 **References.**

566

567 Arasuna, A., Okuno, M., Mizukami, T., Akaogi, M., Yokoyama, T., Okudera, H., and Arai, S.  
568 (2013) The role of water in coesite crystallization from silica gel. *European Journal of*  
569 *Mineralogy*, 25, 791–96.

570 Bromiley, G.D., Bromiley, F.A., and Bromiley, D.W. (2006) On the mechanisms for H and Al  
571 incorporation in stishovite. *Physics and Chemistry of Minerals*, 33, 613–621.

572 Bruker AXS. (2008) TOPAS V4: general profile and structure analysis software for powder  
573 diffraction data – user’s manual. Bruker AXS Inc., Karlsruhe, Germany.

574 Datchi, F., Loubeyre, P., and LeToullec, R. (2000) Extended and accurate determination of the  
575 melting curves of argon, helium, ice (H<sub>2</sub>O) and hydrogen (H<sub>2</sub>). *Physical Review B* 61,  
576 6535–6546.

577 Dubrovinskaia, N., and Dubrovinsky, L. (2003) Melting curve of water studied in externally  
578 heated diamond-anvil cell. *High Pressure Research*, 23, 307-311.

579 Gibbs, G.V., Cox, D.F., and Ross, N.L. (2004) A modeling of the structure and favorable H  
580 docking sites and defects for the high-pressure silica polymorph stishovite. *Physics and*  
581 *Chemistry of Minerals*, 31, 232–239.

582 Hacker, B.R., Peacock, S.M., Abers, G.A., Holloway, S.D. (2003) Subduction factory—2. Are  
583 intermediate-depth earthquakes in subducting slabs linked to metamorphic dehydration  
584 reactions? *Journal of Geophysical Research-Solid Earth*, 108, B12030.

- 585 Hemley, R.J., Mao, H.-K., and Chao, E.C.T. (1986) Raman spectrum of natural and synthetic  
586 stishovite. *Physics and Chemistry of Minerals*, 13, 285–290.
- 587 Hirose, K., Takafuji, N., Sata, N., and Ohishi, Y. (2005) Phase transition and density of subducted  
588 MORB crust in the lower mantle. *Earth and Planetary Science Letters*, 237, 239–251.
- 589 Hofmeister, A.M., Xu, J., and Akimoto, S. (1990) Infrared spectroscopy of synthetic and natural  
590 stishovite. *American Mineralogist*, 75, 951-955.
- 591 Jaeger C. and Hemmann F. (2014) EASY: A simple tool for simultaneously removing  
592 background, deadtime and acoustic ringing in quantitative NMR spectroscopy—Part I:  
593 Basic principle and applications. *Solid State Nuclear Magnetic Resonance*, 57-58, 22-28.
- 594 Järvinen, M. (1993) Application of symmetrized harmonics expansion to correction of the  
595 preferred orientation effect. *Journal of Applied Crystallography*, 26, 25–531.
- 596 Kameyama, T., and Naka, S. (1974) Effect of water on transformation of amorphous silica to  
597 coesite. *Journal of the American Ceramic Society*, 57, 499-499.
- 598 Kolesov, B.A., and Geiger, C.A. (2005) The vibrational spectrum of synthetic hydrogrossular  
599 (katoite)  $\text{Ca}_3\text{Al}_2(\text{O}_4\text{H}_4)_3$ : a low-temperature IR and Raman spectroscopic study. *American*  
600 *Mineralogist*, 90, 1335-1341.
- 601 Lager, G.A., Armbruster, T., and Faber, J. (1987) Neutron and X-ray diffraction study of  
602 hydrogarnet  $\text{Ca}_3\text{Al}_2(\text{O}_4\text{H}_4)_3$ . *American Mineralogist*, 72, 756–765.
- 603 Lee, C., and Gonze, X. (1994) Lattice dynamics and dielectric properties of  $\text{SiO}_2$  stishovite.  
604 *Physical Review Letters*, 72, 1686-1689.

- 605 Libowitzky, E. (1999) Correlation of O–H stretching frequencies and O–H···O hydrogen bond  
606 lengths in minerals. *Monatshefte für Chemie*, 130, 1047-1059.
- 607 Libowitzky, E., and Beran, A. (2006) The Structure of Hydrous Species in Nominally Anhydrous  
608 Minerals: Information from Polarized IR Spectroscopy. *Reviews in Mineralogy and*  
609 *Geochemistry*, 62, 29–52.
- 610 Lin, J.-F., Militzer, B., Struzhkin, V.V., Gregoryanz, E., Hemley, R.J., and Mao, H. (2004) High  
611 pressure-temperature Raman measurements of H<sub>2</sub>O melting to 22 GPa and 900 K. *The*  
612 *Journal of Chemical Physics*, 121, 8423-8427.
- 613 Litasov, K.D., Kagi, H., Shatskiy, A., Ohtani, E., Lakshmanov, D.L., Bass, J.D., and Ito, E. (2007)  
614 High hydrogen solubility in Al-rich stishovite and water transport in the lower mantle.  
615 *Earth and Planetary Science Letters*, 262, 620–634.
- 616 Lityagina, L.M., Dyuzheva, T.I., Nikolaev, N.A., and Bendeliani, N.A. (2001) Hydrothermal  
617 crystal growth of stishovite (SiO<sub>2</sub>). *Journal of Crystal Growth*, 222, 627–629.
- 618 Liu, L., Zhang, J., Green, H.W. II, Jin, Z., Bozhilov, K.N. (2007) Evidence of former stishovite  
619 in metamorphosed sediments, implying subduction to >350 km. *Earth and Planetary*  
620 *Science Letters*, 263, 180–191.
- 621 Naka, S., Inagaki, M., Kameyama, T., and Suwa, K. (1974a) The effect of water on the crystal  
622 growth of coesite. *Journal of Crystal Growth*, 24, 614-616.
- 623 Naka, S., Ito, S., and Inagaki, M. (1974b) Kinetic studies of transitions from amorphous silica  
624 and quartz to coesite. *Journal of the American Ceramic Society*, 57, 217-219.

- 625 Ono, S., Katsura, T., and Ito, E. (2001) Mineralogy of subducted basaltic crust (MORB) from 25  
626 to 37 GPa, and chemical heterogeneity of the lower mantle. *Earth and Planetary Science*  
627 *Letters*, 190, 57–63.
- 628 Pawley, A.R., McMillan, P.F., and Holloway, J.R. (1993) Hydrogen in Stishovite, with  
629 Implications for Mantle Water Content. *Science*, 261, 1024–1026.
- 630 Ricolleau, A., Perrillat, J.P., Fiquet, G., Daniel, D., Matas, J., Addad, A., Menguy, N., Cardon,  
631 H., Mezouar, M., Guignot, N. (2010) Phase relations and equation of state of a natural  
632 MORB: Implications for the density profile of subducted oceanic crust in the Earth's  
633 lower mantle. *Journal of Geophysical Research-Solid Earth*, 115, B08202.
- 634 Rietveld, H.M. (1969) A profile refinement method for nuclear and magnetic structures. *Journal*  
635 *of Applied Crystallography*, 2, 65–71.
- 636 Rodríguez-Carvajal, J. (1990) FULLPROF: A Program for Rietveld Refinement and Pattern  
637 Matching Analysis. Abstracts of the Satellite Meeting on Powder Diffraction of the XV  
638 IUCr Congress (1990), 127.
- 639 Rossman, G.R., and Aines, R.D. (1991) The hydrous components in garnets: Grossular-  
640 hydrogrossular. *American Mineralogist*, 76, 1153–1164.
- 641 Rossman, G.R. (2006) Analytical Methods for Measuring Water in Nominally Anhydrous  
642 Minerals. *Reviews in Mineralogy and Geochemistry*, 62, 1-28.

- 643 Sabine, T.M., Hunter, B.A., Sabine, W.R., and Ball, C.J. (1998) Analytical Expressions for the  
644 Transmission Factor and Peak Shift in Absorbing Cylindrical Specimens. *Journal of*  
645 *Applied Crystallography*, 31, 47–51.
- 646 Shatskiy, A., Yamazaki, D., Borzdov, Y.M., Matsuzaki, T., Litasov, K.D., Cooray, T., Ferot, A.,  
647 Ito, E., and Katsura, T. (2010) Stishovite single-crystal growth and application to silicon  
648 self-diffusion measurements. *American Mineralogist*, 95, 135–143.
- 649 Smyth, J.R., Swope, R.J., Pawley, A.R. (1995) H in rutile-type compounds: II. Crystal chemistry  
650 of Al substitution in H-bearing stishovite. *American Mineralogist*, 80, 454–456.
- 651 Spektor, K., Nylen, J., Stoyanov, E., Navrotsky, A., Hervig, R.L., Leinenweber, K., Holland,  
652 G.P., and Häussermann, U. (2011) Ultrahydrous stishovite from high-pressure  
653 hydrothermal treatment of SiO<sub>2</sub>. *Proceedings of the National Academy of Sciences*, 108,  
654 20918–20922.
- 655 Stoyanov, E., Häussermann, U., and Leinenweber, K. (2010) Large-volume multianvil cells  
656 designed for chemical synthesis at high pressures. *High Pressure Research*, 30, 175–189.
- 657 Thomas, S.M., Koch-Müller, M., Reichart, P., Rhede, D., Thomas, R., Wirth, R., Matsyuk, S.  
658 (2009) IR calibrations for water determination in olivine, r-GeO<sub>2</sub>, and SiO<sub>2</sub> polymorphs.  
659 *Physics and Chemistry of Minerals*, 36, 489–509.
- 660 Wöhlecke, M., Kovacs, L. (2001) OH<sup>-</sup> ions in oxide crystals. *Critical Reviews in Solid State and*  
661 *Material Sciences*, 25, 1–86.

662 Zhang, G., Xu, Y., Xu, D., Wang, D., Xue, Y., and Su, W. (2008) Pressure-induced  
663 crystallization of amorphous SiO<sub>2</sub> with silicon–hydroxy group and the quick synthesis of  
664 coesite under lower temperature. High Pressure Research, 28, 641-650.

665 Zhang, J., Li, B., Utsumi, W., and Liebermann, R.C. (1996) In situ X-ray observations of the  
666 coesite-stishovite transition: reversed phase boundary and kinetics. Physics and  
667 Chemistry of Minerals, 23, 1–10.

668

669

670

671 **Figures.**

672

673 Figure 1. (a) PXRD patterns of products obtained from an 8 hour hydrothermal treatment of  
674 silica glass at 10 GPa and temperatures from 350 to 550 °C. Bragg reflections for anhydrous  
675 stishovite are emphasized by vertical dotted lines and indexed. The arrow indicates the strongest  
676 reflection of coesite in the 350 °C product. (b) Trend of the 220 reflection. The 350 and 400  
677 samples represent of two-phase mixtures.

678

679 Figure 2. (a) PXRD patterns of the coe-400, 450-15min, and 450-D2O samples. (b) Location and  
680 shape of the 220 reflection in the PXRD pattern for various samples obtained at 450 °C (the  
681 patterns for 400 and 500 are shown for comparison). The vertical dotted line marks the position  
682 of 220 in anhydrous stishovite.

683

684 Figure 3: SEM images of the 350, 400, 450, 500, 550, and anhydrous samples. 350: a bulk  
685 agglomerate having an appearance of a glass piece in the starting material (left) and intergrown  
686 stishovite crystals the surface of an agglomerate (right). 400: agglomerate of partially separated  
687 stishovite crystals (left) and close-up of these crystals displaying a rounded tabular appearance  
688 (right). 450: separated crystals showing with visible intergrowth contacts. 500: crystals with  
689 various morphologies and sizes. 550: evenly sized euhedral crystals with sharp edges.  
690 Anhydrous: stishovite crystals grown by slow cooling from 1000 °C.

691

692 Figure 4. SEM images of the 450-15min sample: (a) separated crystals after transformation; (b)  
693 stishovite particles peeling off a large coesite crystal; (c) coesite crystal with sub-micrometer  
694 sized bulky particles attached to the surface; (d) overview of flat rounded stishovite crystals.

695

696 Figure 5. (a) DSC and (b) TGA traces for various hydrous stishovite samples and anhydrous  
697 stishovite.

698

699 Figure 6. Rietveld plots for the PXRD patterns of (a) the 400 sample (two-phase mixture), (b) the  
700 500 sample refined as single phase stishovite, and (c) the 500 sample refined as two-phase  
701 mixture.

702

703 Figure 7. (a) Crystal structure of rutile-type stishovite. Si and O atoms are depicted as red and  
704 grey circles, respectively.  $\text{SiO}_6$  octahedra share edges in the *c* direction and corners in the *ab*  
705 plane. (b) Nearest neighbor interatomic distances in the stishovite structure (3 different O–O and  
706 2 different Si–O). The values (in Å) refer to anhydrous stishovite (in parentheses) and hydrous  
707 stishovite (phase h+ in sample 400).

708

709 Figure 8. (a) Raman spectra of the 450 and anhydrous stishovite samples. The peaks at  $520\text{ cm}^{-1}$   
710 and  $900\text{ cm}^{-1}$  in the anhydrous spectrum stem from a small amount of coesite impurity. (b) FTIR  
711 spectra of the 350, 400, 450-D<sub>2</sub>O (red line), 450, 500, 550, and anhydrous stishovite samples  
712 showing the wavenumber range of Si–O vibrations. The indicated TO – LO split of IR modes is  
713 according to the calculations by Lee and Gonze (1994).

714

715 Figure 9. (a) FTIR spectra of various hydrous stishovite samples in the spectral range of O–H  
716 vibrations. (b) FTIR spectra of the 450-D<sub>2</sub>O sample (red) and the 450 sample (black).

717

718 Figure 10. Temperature dependent FTIR spectra of the 450 sample in the spectral range of the  
719 O–H vibrations. Note that the spectra are uncorrected reflectance data. The location of bands  
720 deviates somewhat from Figure 9.

721

722 Figure 11. <sup>1</sup>H MAS NMR spectra recorded from the 450 sample at temperatures of 30 °C (red  
723 traces) and 110 °C (black traces). The spectrum in (b) is a zoom of that in (a). The dotted lines  
724 mark signals assigned to unique sites of the stishovite structure: note that the resonances around  
725 9.4 ppm and 10.8 ppm are present in both spectra (but exhibit distinct relative intensities at the  
726 different temperatures).

727

728

729

730

731

732  
 733  
 734  
 735  
 736

**Tables.**

Table 1. Experimental conditions and synthesis products

Run and sample label	Synthesis temperature	Starting material	Heating duration	Product
350	350 °C	SiO <sub>2</sub> glass powder+H <sub>2</sub> O	8 h	<i>h+</i> and <i>h-</i> stishovite, coesite
400	400 °C	SiO <sub>2</sub> glass powder+H <sub>2</sub> O	8 h	<i>h+</i> and <i>h-</i> stishovite
400-coe	400 °C	Coesite sintered pieces + H <sub>2</sub> O	8h	<i>h+</i> and <i>h-</i> stishovite
450-coe*	400 °C	Coesite sintered pieces + H <sub>2</sub> O	8h	single phase hydrous stishovite
450*	450 °C	SiO <sub>2</sub> glass powder+H <sub>2</sub> O	8 h	single phase hydrous stishovite
450-10h	450 °C	SiO <sub>2</sub> glass powder+H <sub>2</sub> O	10 h	<i>h+</i> and <i>h-</i> stishovite
450-D2O	450 °C	SiO <sub>2</sub> glass powder+D <sub>2</sub> O	8 h	<i>d+</i> and <i>d-</i> stishovite
450-15min	450 °C	SiO <sub>2</sub> glass powder +H <sub>2</sub> O	15 min	single phase hydrous stishovite, coesite
500	500 °C	SiO <sub>2</sub> glass powder+H <sub>2</sub> O	8 h	single phase hydrous stishovite
550*	550 °C	SiO <sub>2</sub> glass powder+H <sub>2</sub> O	8 h	single phase hydrous stishovite
anhydrous	Slow cooling from 1000 °C to 500 °C, 1 °C /min	SiO <sub>2</sub> glass powder+H <sub>2</sub> O (1:2.5)	≈8.3 h	single phase anhydrous stishovite

737  
 738  
 739  
 740  
 741  
 742  
 743  
 744  
 745  
 746  
 747

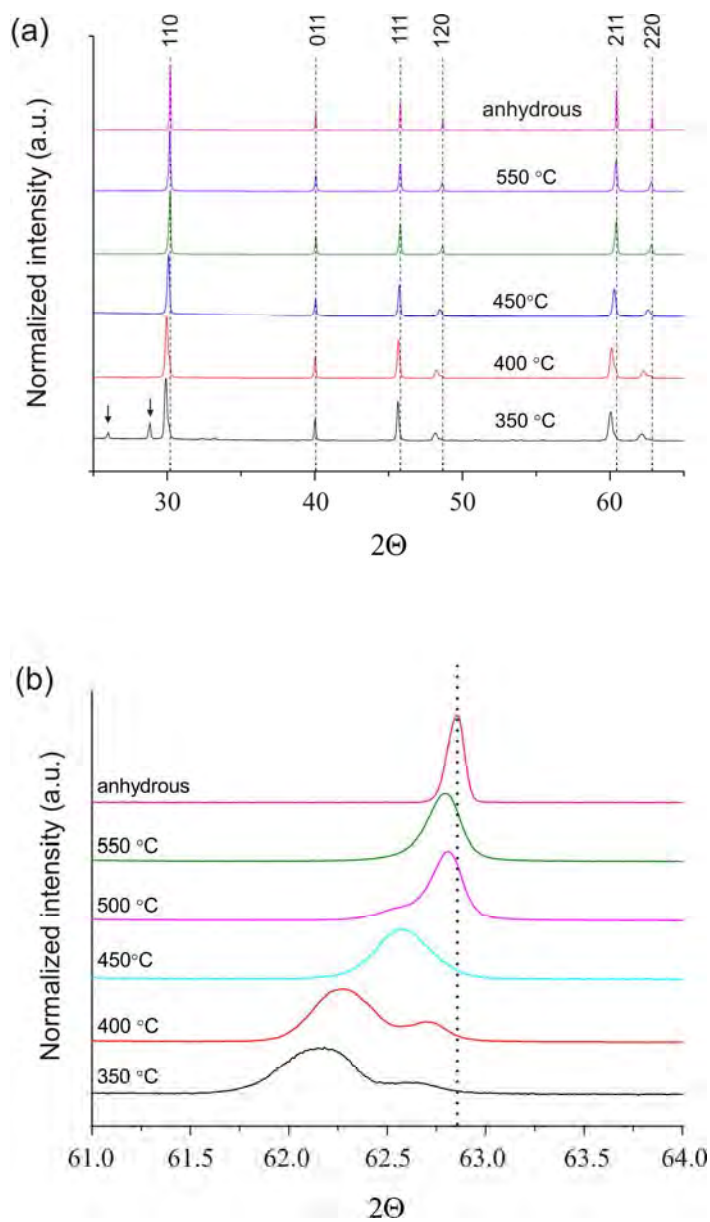
\*already described in Spektor et al. (2011).

748 Table 2. Crystal data and refinement results (data of samples marked with an asterisk were only  
 749 subjected to Pawley fitting)

Sample ID	<i>a</i> (Å)	<i>c</i> (Å)	<i>V</i> (Å <sup>3</sup> )	<i>x</i> (O)	<i>B</i> <sub>iso</sub> (Si)	<i>B</i> <sub>iso</sub> (O)	<i>R</i> <sub>p</sub> (%)	<i>R</i> <sub>wp</sub> (%)	<i>R</i> <sub>f</sub> (%)	<i>R</i> <sub>bragg</sub> (%)	Weight %
*350 h+	4.2194(2)	2.6610(2)	47.37				5.09	7.34		1.04	~82
*350 h-	4.1911(2)	2.6647(2)	46.81				5.09	7.34		1.50	~18
400 h+	4.2123(1)	2.6619(1)	47.23	0.3090(6)	0.79(5)	0.49(8)	8.83	10.0	1.41	2.50	78(<1)
400 h-	4.1872(2)	2.6640(2)	46.71	0.3035(17)	0.79(5)	0.49(8)	8.83	10.0	1.71	2.66	22(<1)
*400-coe h+	4.2261(2)	2.6646(2)	47.59				4.95	7.09		0.75	47
*400-coe h-	4.1965(2)	2.6654(2)	46.94				4.95	7.09		0.93	53
*450-15min	4.2066(2)	2.6642(2)	47.14				5.70	8.83		1.48	88
450-8h	4.1966(1)	2.6650(1)	46.94	0.3087(6)	1.44(8)	1.47(12)	13.2	9.44	1.09	1.81	100
450-10h h+	4.1980(1)	2.6637(1)	46.94	0.3080(9)	1.25(5)	1.33(9)	13.4	12.3	2.91	4.48	50(1)
450-10h h-	4.1873(1)	2.6646(1)	46.72	0.3071(9)	1.25(5)	1.37(9)	13.4	12.3	2.45	4.35	50(1)
450-D2O d+	4.2084(2)	2.6629(1)	47.16	0.3117(13)	1.25(7)	1.30(12)	11.4	11.1	2.63	4.22	52(<1)
450-D2O d-	4.1849(2)	2.6643(2)	46.66	0.3073(13)	1.25(7)	1.30(12)	11.4	11.1	2.38	4.50	48(<1)
500 single phase	4.1810(1)	2.6651(1)	46.59	0.3074(7)	0.54(7)	0.64(11)	9.05	11.7	1.68	3.09	100
500 double phase h+	4.1954(1)	2.6630(2)	46.87	0.3083(17)	0.66(2)	0.72(2)	5.69	6.38	1.64	2.99	12(<1)
500 double phase h-	4.1804(1)	2.6649(1)	46.57	0.3069(3)	0.66(2)	0.72(2)	5.69	6.38	1.15	2.14	88(<1)
550	4.1812(1)	2.6647(1)	46.59	0.3074(4)	0.60(4)	0.71(7)	6.95	7.70	1.40	3.02	100
Anhydrous	4.1775(1)	2.6654(1)	46.52	0.3067(4)	0.40(4)	0.58(6)	11.7	12.3	2.73	4.83	100

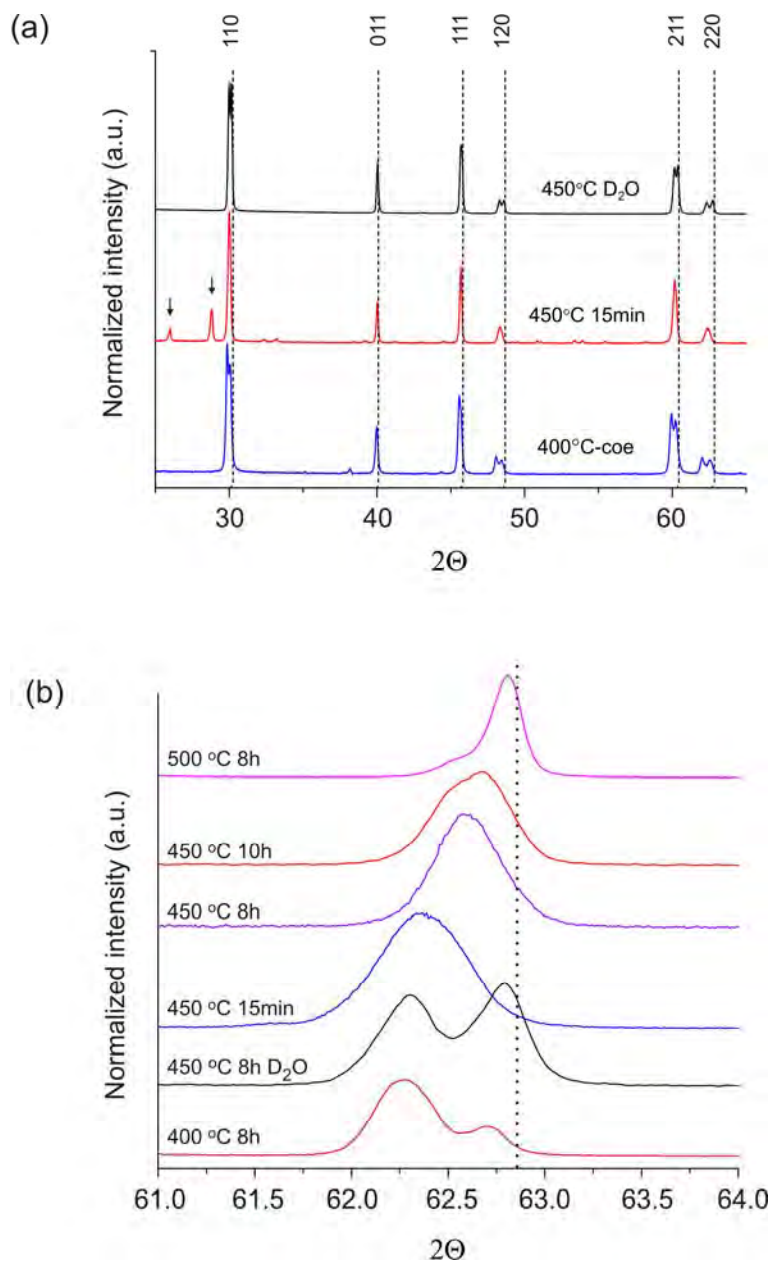
750  
 751  
 752  
 753

754 Figure 1  
755  
756



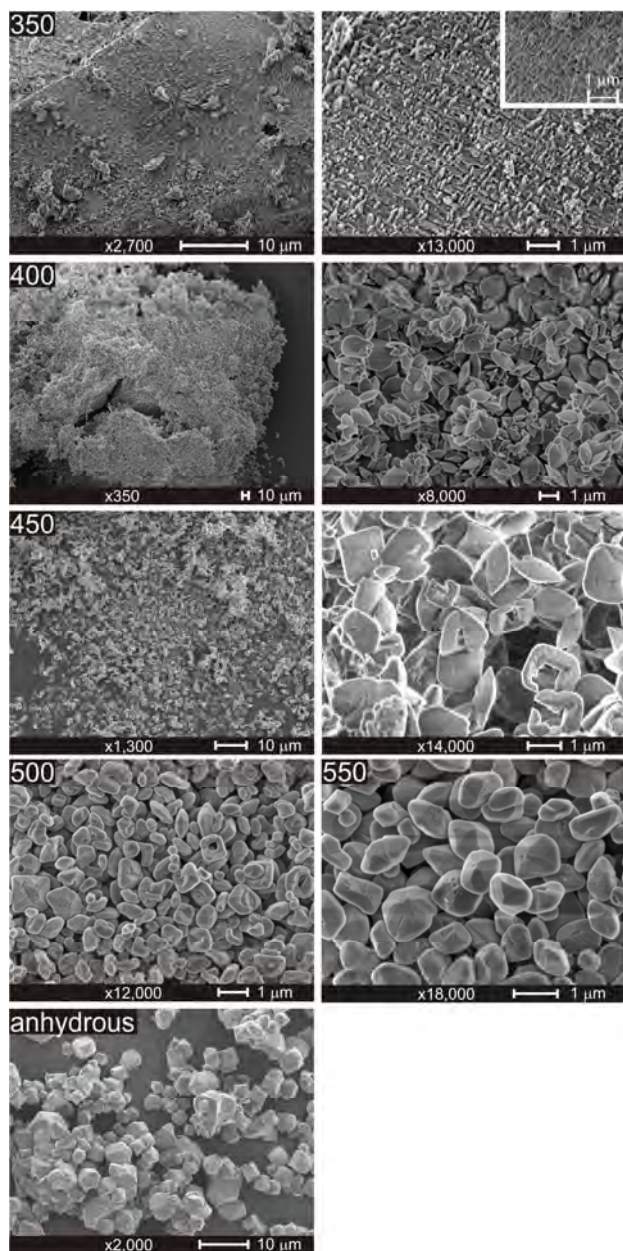
757  
758

759 Figure 2  
760  
761



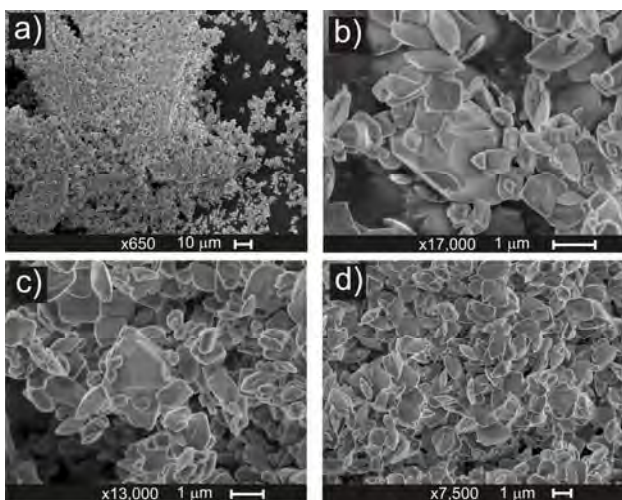
762  
763

764 Figure 3.  
765  
766



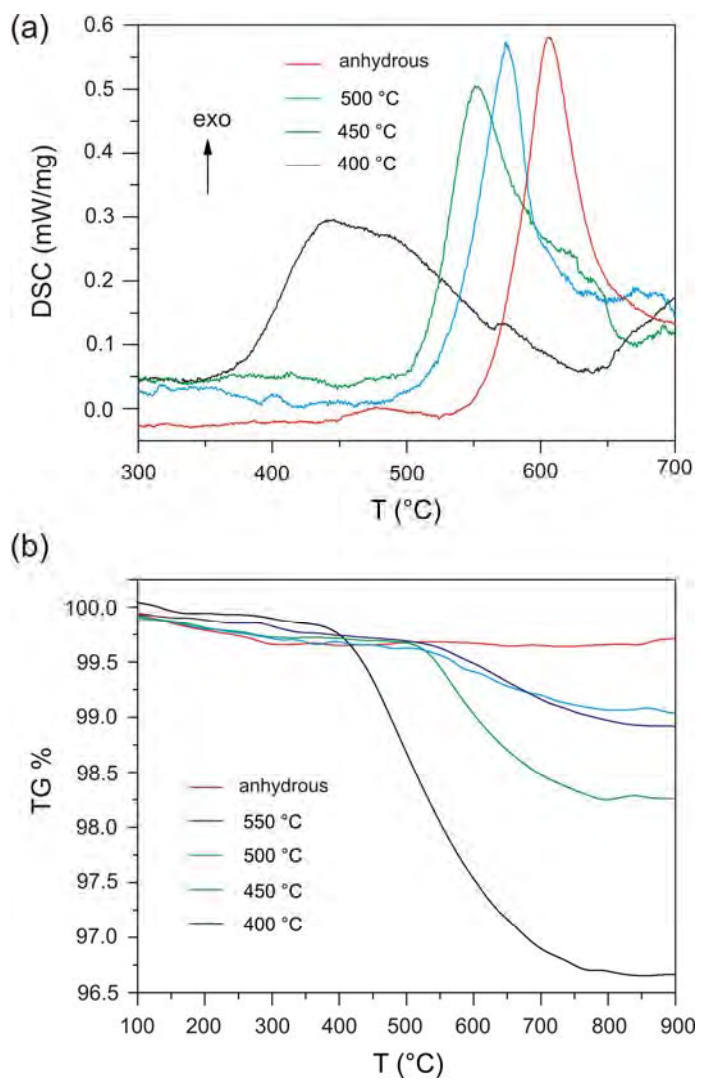
767  
768  
769

770 Figure 4.  
771  
772



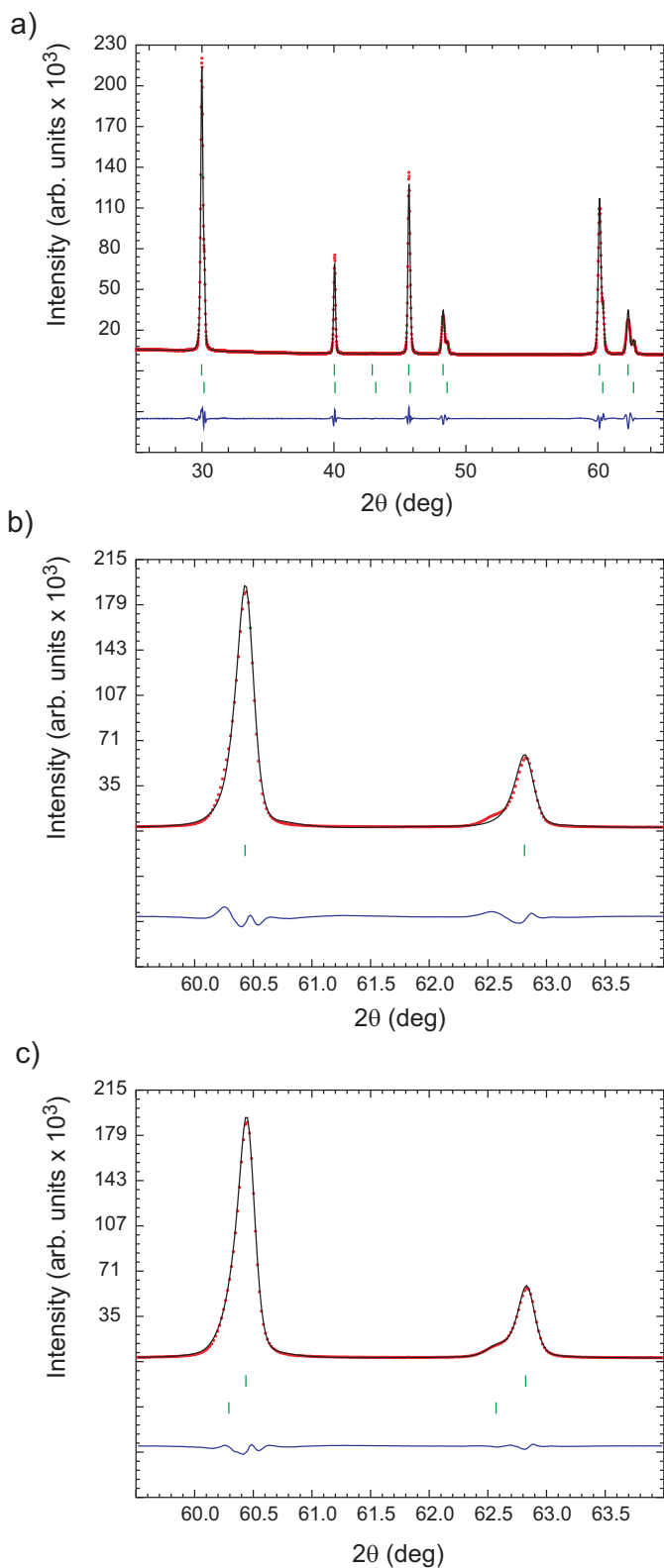
773  
774  
775  
776

777 Figure 5  
778  
779



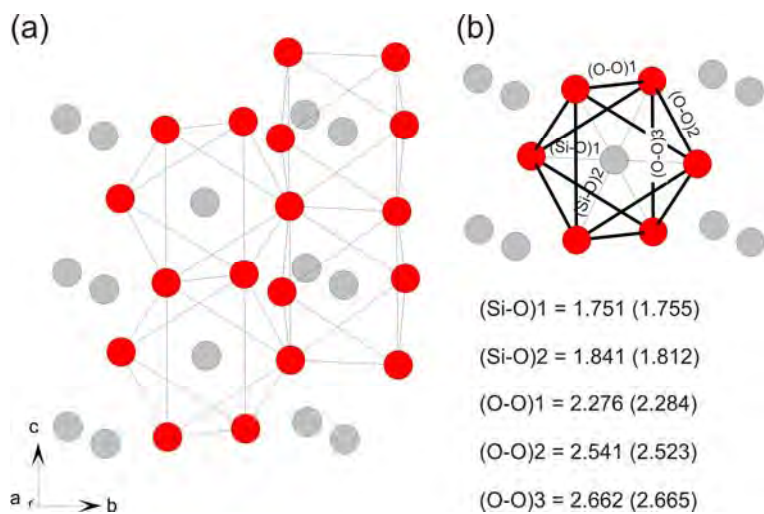
780  
781  
782  
783  
784

785 Figure 6  
786  
787



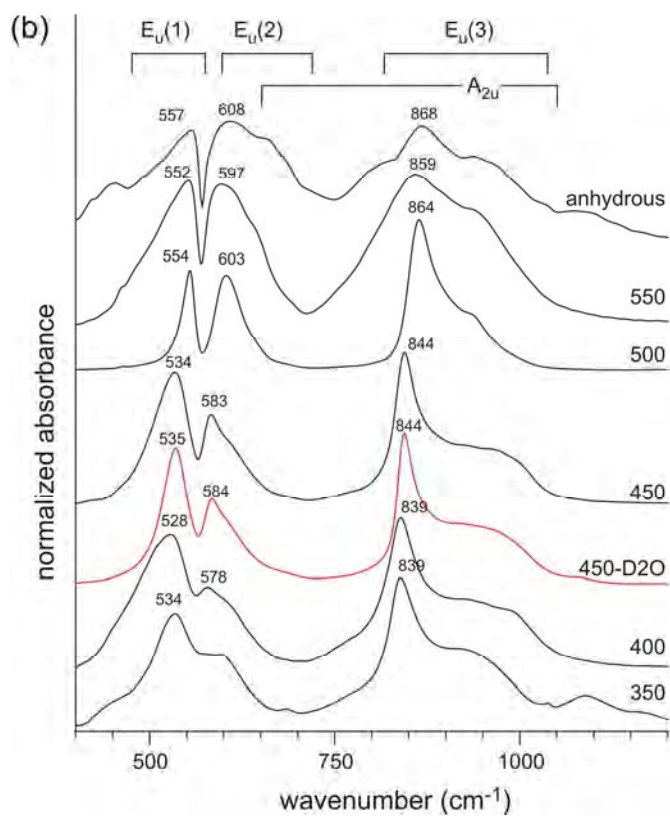
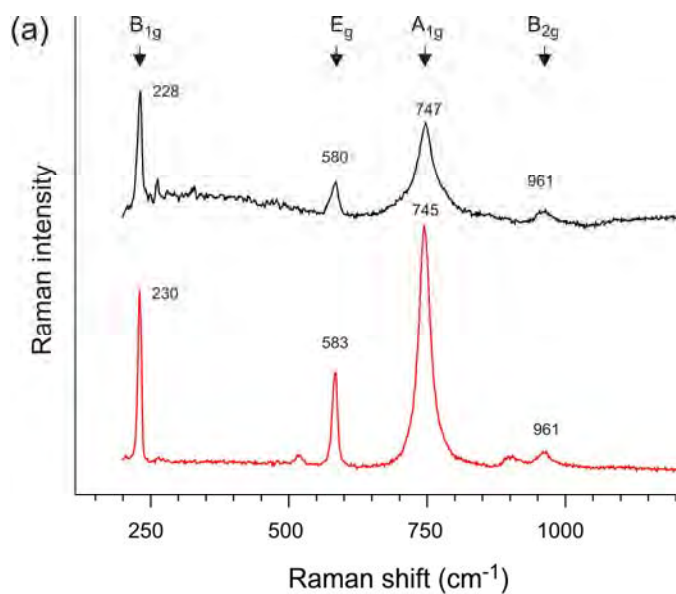
788  
789

790 Figure 7  
791  
792



793  
794  
795  
796  
797

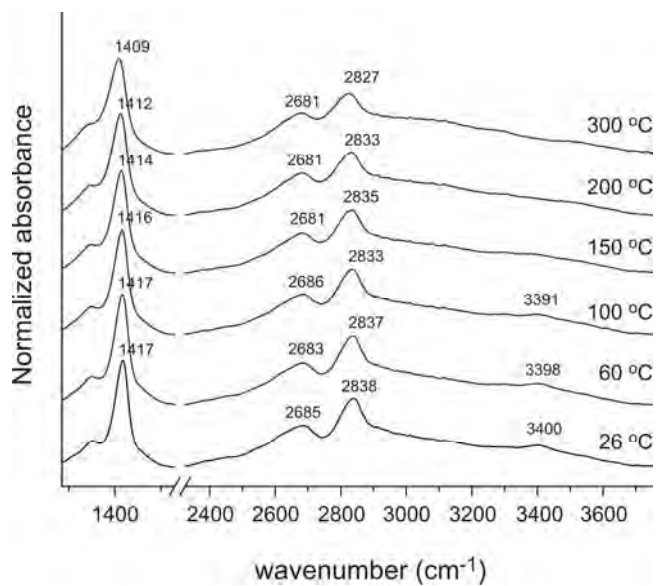
798 Figure 8  
799  
800



801  
802  
803  
804

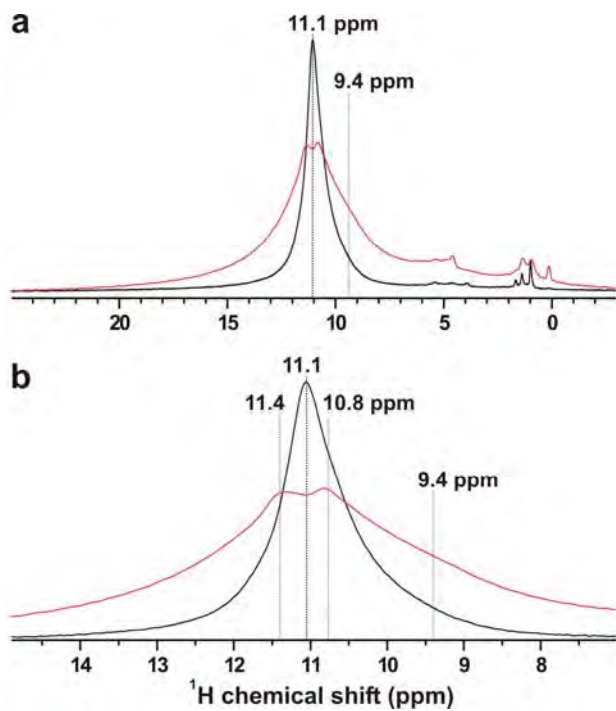


810 Figure 10  
811  
812



813  
814  
815  
816  
817  
818

819 Figure 11:  
820  
821



822  
823  
824  
825